Solid State Ionics 326 (2018) 18–26

Contents lists available at ScienceDirect

Solid State Ionics

journal homepage: www.elsevier.com/locate/ssi

Facile solvothermal synthesis of $Na_{1.5}\square_{0.5}Mn_{1.5}Fe_{1.5}(PO_4)_3$: Electrochemical study as a dual electrode material for lithium-ion batteries

Claude Karegeya[a,b], Abdelfattah Mahmoud[a,*], Frédéric Hatert[c], Rudi Cloots[a], Bénédicte Vertruyen[a], Pierre Emmanuel Lippens[d], Frédéric Boschini[a]

[a] GREENMAT, CESAM, Institute of Chemistry B6, University of Liège, 4000 Liège, Belgium
[b] Faculty of Sciences, College of Education, University of Rwanda, 5039 Kigali, Rwanda
[c] Laboratory of mineralogy B18, University of Liège, 4000 Liège, Belgium
[d] Institut Charles Gerhardt, UMR 5253 CNRS, Université de Montpellier, Place Eugène Bataillon, 34095 Montpellier cedex 5, France

ARTICLE INFO

Keywords:
Electrochemistry
Dual electrode material
Conversion reaction
Alluaudite
$Na_{1.5}\square_{0.5}Mn_{1.5}Fe_{1.5}(PO_4)_3$
Mossbauer spectroscopy

ABSTRACT

$Na_{1.5}\square_{0.5}Mn_{1.5}Fe_{1.5}(PO_4)_3$ (where □ denotes vacancies) microrods were obtained through a solvothermal synthesis in ethylene glycol. The combination of the XRD, Mössbauer and magnetic analyses confirm that the sodium vacancies in the $Na_{1.5}\square_{0.5}Mn_{1.5}Fe_{1.5}(PO_4)_3$ structure are linked to the oxidation of Mn and Fe transition metals. The electrochemical tests have shown that $Na_{1.5}\square_{0.5}Mn_{1.5}Fe_{1.5}(PO_4)_3$ is a dual electrode material for Li-ion batteries. The electrochemical study in the potential range of 1.5–4.5 V indicate that such material can be used as 3 V cathode with specific capacities of 109, 97, and 80 $mAh{\cdot}g^{-1}$ at current densities of 5, 10, and 20 $mA{\cdot}g^{-1}$, respectively. When it is tested in the potential range of 0.03–3.0 V as negative electrode material, it delivers a reversible capacity of about 170 $mAh{\cdot}g^{-1}$ at 200 $mA{\cdot}g^{-1}$ current density during > 100 cycles.

1. Introduction

Iron phosphate-based alluaudite materials have recently attracted increasing attention as promising cathode materials for next-generation lithium-ion batteries (LIBs) and sodium-ion batteries (NIBs), or in hybrid-ion batteries (HIBs) where a sodium-containing pristine cathode material is cycled with a Li-based electrolyte [1–4]. The importance given to this alluaudite group is due to their stability at high temperature, the presence of vacancies allowing easy intercalation of many Na^+/Li^+-ions in their crystal structures, excellent cyclability as well as their environmental friendliness and low cost [3,5,6]. Due to their high molecular weight, phosphate based alluaudites have generally rather low theoretical capacities. However, the existence of vacancies owing to their complementarily and synergetic effect in the insertion/extraction process may enhance their specific capacities and ensures good cycling performances as cathode materials for HIBs, LIBs and NIBs. Due to the low conductivity of iron based phosphate materials, various techniques have been used such as coatings, formation of composites with conducting materials to enhance their conductivity and improve electrochemical performances of these materials in LIBs and NIBs [7–10].

The $Na_{1.5}\square_{0.5}Mn_{1.5}Fe_{1.5}(PO_4)_3$ compound (where □ denotes vacancies) was previously obtained by F. Hatert et al. by solid state synthesis route to investigate its crystallographic structure [11,12]. In addition, they proposed this material may be among the promising electrodes for LIBs and NIBs due to the interesting properties presented by the iron phosphate-based alluaudite materials as detailed above. However, the solid state synthesis offers less morphology and composition control than wet chemistry approaches [13–15].

In the recent years, a large number of solvothermal syntheses have emerged for iron-phosphate materials [16–20] that offer many advantages such as low temperature processes, fast reaction kinetics, short processing times, phase purity, high crystallinity, high yield, homogeneous particle products, composite formation, narrow particle-size distributions, low temperature post-calcinations, and they are cost effective, environmentally benign, and easily scalable [2]. Herein, a facile approach for the synthesis of $Na_{1.5}\square_{0.5}Mn_{1.5}Fe_{1.5}(PO_4)_3$ microrods was designed using a solvothermal route in ethylene glycol. Due to the interesting properties of iron phosphate-based alluaudite phases from their vacancy rich crystal structure, $Na_{1.5}\square_{0.5}Mn_{1.5}Fe_{1.5}(PO_4)_3$ has attracted our attention and we report in the present work this phase obtained by solvothermal synthesis route to meet the morphology and size requirements for the fabrication of cathode materials with excellent electrochemical performance [1,21,22]. The solvothermal synthesis of $Na_{1.5}\square_{0.5}Mn_{1.5}Fe_{1.5}(PO_4)_3$ was followed by heat treatment to obtain samples with high crystallinity and small particle size. This may

* Corresponding author.
E-mail address: abdelfattah.mahmoud@ulg.ac.be (A. Mahmoud).

https://doi.org/10.1016/j.ssi.2018.09.004
Received 28 May 2018; Received in revised form 5 September 2018; Accepted 10 September 2018
Available online 18 September 2018

facilitate the penetration of electrolyte and lithium ions in electrode material, and could provide much more active sites. This may enhance the electrochemical performances of active material and, therefore can provide fast transport channels and reduce diffusion paths of lithium ions [23,24].

The aim of this work is to synthesize $Na_{1.5}\square_{0.5}Mn_{1.5}Fe_{1.5}(PO_4)_3$ as new electrode material for lithium-ion batteries through wet chemical synthesis in ethylene glycol (EG). EG as a reaction medium, plays an important role in both reducing the particle size and product defects [25]. The high thermal stability of iron phosphate-based alluaudite compounds and the vacancies in $Na_{1.5}\square_{0.5}Mn_{1.5}Fe_{1.5}(PO_4)_3$ structure are the main reasons for this material to deliver excellent electrochemical performance (cycling stability and rate capability). Additionally, the strong inductive effect of the $(PO_4)^{3-}$ polyanion group moderates the energetics of the transition metal redox couple to generate their relatively high operating potentials as positive electrode. Recently R. Essehli et al. showed that iron phosphate-based materials also possess low active voltage for negative electrode application and these characteristics qualify $Na_{1.5}\square_{0.5}Mn_{1.5}Fe_{1.5}(PO_4)_3$ as dual electrode materials [26,27]. All above described properties make this material an attracting candidate electrode with promising electrochemical properties.

2. Experimental

2.1. Chemicals

Ammonium dihydrogen phosphate ($NH_4H_2PO_4$, ≥ 99%, Acros), manganese nitrate ($Mn(NO_3)_2$, 99.98%, Alfa Aesar), hydrated iron(III) nitrate ($Fe(NO_3).9H_2O$, 96%, Riedel-de Haën), sodium nitrate ($NaNO_3$, ≥ 90.0%, Sigma- Aldrich) and ethylene glycol as the solvent were used as received without further purification.

2.2. Material synthesis

Uniform $Na_{1.5}\square_{0.5}Mn_{1.5}Fe_{1.5}(PO_4)_3$ microrods were successfully obtained by a solvothermal method in ethylene glycol. In this synthesis, $NH_4H_2PO_4$, $Mn(NO_3)_2$, $Fe(NO_3)_3.9H_2O$ and $Na(NO_3)$ solutions in ethylene glycol were mixed in a molar ratio of 3:2:2:4. The solution of 6 mmol $NH_4H_2PO_4$, 4 mmol $Mn(NO_3)_2$, 4 mmol $Fe(NO_3)_3.6H_2O$ and 8 mmol $NaNO_3$ dissolved in 60 ml of ethylene glycol was mixed vigorously for about 20 min. The reaction mixture was then sealed into a 125 ml teflon-lined stainless steel autoclave, sealed and heated at 180 °C for 6 h in oven. After cooling down to the room temperature,-apple green precipitate was obtained and washed three times with ethanol and water respectively. The powder product was dried in oven under vacuum for two hours at 80 °C and post calcined at 700 °C for 48 h under air to remove remaining ethylene glycol and achieve a highly crystallized and pure phase of $Na_{1.5}\square_{0.5}Mn_{1.5}Fe_{1.5}(PO_4)_3$.

Fig. 1 shows the low temperature solvothermal synthesis approach of $Na_{1.5}\square_{0.5}Mn_{1.5}Fe_{1.5}(PO_4)_3$. We have used ethylene glycol (EG) to decrease the solubility of the precursors, increase the number of nucleation sites, and thereby achieve smaller particle dimensions [21].

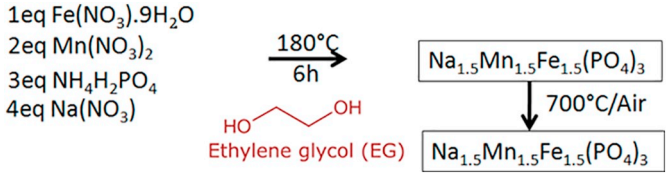

Fig. 1. Schematic representation of the solvothermal synthesis process of $Na_{1.5}\square_{0.5}Mn_{1.5}Fe_{1.5}(PO_4)_3$.

2.3. Characterizations

The synthesized samples were characterized by powder X-ray diffraction (XRD) using a Bruker D8 diffractometer (Cu Kα radiation). ^{57}Fe transmission Mössbauer spectroscopy data were recorded by using a constant-acceleration spectrometer with a ^{57}Co (Rh) source at room temperature. The Mössbauer spectral absorbers were prepared with 30 mg of $Na_{1.5}\square_{0.5}Mn_{1.5}Fe_{1.5}(PO_4)_3$ materials mixed with boron nitride. The spectrometer was calibrated at room temperature with the magnetically split sextet spectrum of a high-purity α-Fe foil as the reference absorber. The measurements were carried out in the velocity ranges a (± 4 mm/s) with optimal energy resolution. The Mössbauer spectra were fitted using one or two Lorentzian doublets using Fullham program. In this way, spectral parameters such as quadrupole splitting (Δ), isomer shift (δ), linewidth (Γ) and relative resonance areas of the different spectral components were determined. The validity of fits was judged on the basis of minimizing the number of parameters and χ^2 values.

The morphology and particle size of $Na_{1.5}\square_{0.5}Mn_{1.5}Fe_{1.5}(PO_4)_3$ samples were investigated by scanning electron microscopy. The SEM analysis of the $Na_{1.5}\square_{0.5}Mn_{1.5}Fe_{1.5}(PO_4)_3$ samples was performed on a FEG-ESEM XL30 (FEI) with an accelerating voltage of 15 kV under high vacuum. $Na_{1.5}\square_{0.5}Mn_{1.5}Fe_{1.5}(PO_4)_3$ powder samples were deposited on carbon tapes. Sputtering deposition was done with gold target under argon atmosphere (Balzers, SCD004, Sputter coater).

Electrochemical measurements were performed using coin cells assembled in an argon-filled glovebox. For preparing working electrodes, a mixture of $Na_{1.5}\square_{0.5}Mn_{1.5}Fe_{1.5}(PO_4)_3$ nanostructures, acetylene black, and polyvinylidene fluoride (PVDF) at a weight ratio of 60:20:20 was pasted on stainless steel grids. The average mass loading was around 1.8 $mg{\cdot}cm^{-2}$. In a typical cell, pure lithium foil served as counter electrode, and microporous polypropylene, 25 mm monolayer films served as separator between electrodes. The electrolyte consisted of a solution of 1 M $LiPF_6$ in ethylene carbonate (EC)/dimethyl carbonate (DMC)/diethyl carbonate (DEC) (1:1:1, in wt%). Galvanostatic cycling tests of the assembled cells were carried out on Neware (China) system in the voltage ranges of 1.5–4.5 V and 0.03–3.0 V (vs Li^+/Li) for positive and negative electrode, respectively.

3. Results and discussions

3.1. Material structure analysis

X-ray powder diffraction was used to investigate the structural properties and to check the phase purity. The crystal structure of $Na_{1.5}\square_{0.5}Mn_{1.5}Fe_{1.5}(PO_4)_3$ was characterized by X-ray diffraction and the corresponding XRD pattern is shown in Fig. 2. All the diffraction peaks can be well indexed according to an alluaudite structure and *C2/c* space group. No impurities such as $FePO_4$ and others, which often appear in the iron phosphate based phases synthesized by traditional routes at high temperature, are detected; there is no observable evidence of secondary phases. The $Na_{1.5}\square_{0.5}Mn_{1.5}Fe_{1.5}(PO_4)_3$ sample obtained after calcination at 700 °C (NMFP-700 °C) shows sharp peaks indicating high crystallinity [28].

The Rietveld refinement of the XRD pattern of $Na_{1.5}\square_{0.5}Mn_{1.5}Fe_{1.5}(PO_4)_3$ was realized, and the experimental details are given in Table 1. Atomic coordinates and temperature factors are given in Table 2; they are in good agreement with those previously reported by Hatert et al. [11,12]. Site occupancy factors indicate that vacancies occur on the A(2)' site (Table 2), in good agreement with the ideal formula of the compound. The A(1) site is filled by Na, the M(1) site is filled by Mn, while the M(2) site contains 0.75 Fe^{3+} and 0.21 Mn. The structural formula of the compound, calculated from the refined site occupancies (Table 2), corresponds to $(Na_{0.64}[]_{0.36})(Na_{0.99}[]_{0.01})(Mn_{0.93}[]_{0.07})(Fe^{3+}_{1.50}Mn_{0.42}[]_{0.08})(PO_4)_3$.

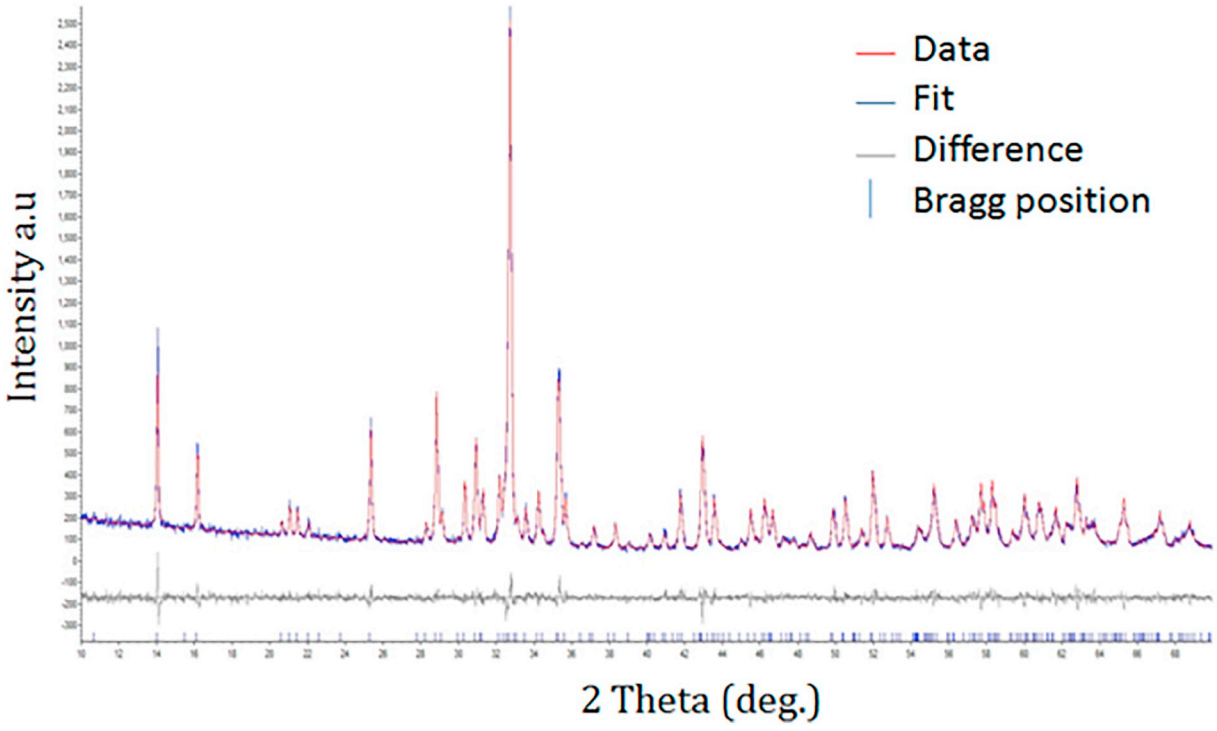

Fig. 2. Final observed, calculated, and difference plots for XRD (CuKα radiation) Rietveld refinement of $Na_{1.5}\square_{0.5}Mn_{1.5}Fe_{1.5}(PO_4)_3$ obtained by solvothermal synthesis.

Table 1
Experimental details for the Rietveld refinement of $Na_{1.5}\square_{0.5}Mn_{1.5}Fe_{1.5}(PO_4)_3$.

Number of reflexions	198
Refined parameters	57
Positional	27
Population	4
Thermal	2
Cell parameters	4
Profile	4
Background	7
Crystallite size, zero point, sample displacement, LP factor, roughness, absorption, thickness, scale factor	9
Space group	*C2/c*
a (Å)	12.070(1)
b (Å)	12.641(1)
c (Å)	6.480(6)
β (°)	114.391(2)
R_p (%)	7.54
$R_{wp\ (\%)}$	9.67
$R_{exp.}$ (%)	8.12
S (GooF)	1.19
R_{Bragg} (%)	1.61

3.2. Mössbauer spectroscopy

The oxidation state, the local environment of Fe and the relative amounts of Fe containing phases were studied by ^{57}Fe Mössbauer spectroscopy. The ^{57}Fe Mössbauer spectrum of $Na_{1.5}\square_{0.5}Mn_{1.5}Fe_{1.5}(PO_4)_3$ sample, measured at room temperature, is shown in Fig. 3. The values of the hyperfine Mössbauer parameters: isomer shift δ, full width at half-maximum Γ, and quadrupole splitting Δ, are reported in Table 3. The Mössbauer spectrum of $Na_{1.5}\square_{0.5}Mn_{1.5}Fe_{1.5}(PO_4)_3$ material shows a symmetric doublet. The spectrum is consistent with the presence of paramagnetic iron, confirming the paramagnetic behavior of the material at room temperature, the lack of magnetic ordering proves also the absence of magnetic iron oxides based impurities at the 1 Fe-at.% level, in good agreement

Table 2
Positional (*x*,*y*,*z*), isotropic thermal (*B*) and site occupancy (*N*) parameters for $Na_{1.5}\square_{0.5}Mn_{1.5}Fe_{1.5}(PO_4)_3$.

Atom	Wyckoff	*X*	*Y*	*Z*	*B* (Å^2)	*N*
Na (A2′)	4*e*	0	−0.010(2)	1/4	1.0	0.64(2)
Na (A1)	4*b*	½	0	0	1.0	0.99(2)
Mn (M1)	4*e*	0	0.2660(5)	1/4	1.0	0.93(1)
Fe/Mn (M2)	8*f*	0.2778(4)	0.6545(3)	0.3637(8)	1.0	0.75/ 0.21(1)
P1	4*e*	0	−0.2825(8)	¼	1.9(3)	1.0
P2	8*f*	0	¾	0.069(1)	1.9(3)	1.0
O1	8*f*	0.453(1)	0.712(1)	0.534(2)	1.1(3)	1.0
O2	8*f*	0.099(1)	0.6407(9)	0.241(2)	1.1(3)	1.0
O3	8*f*	0.334(1)	0.667(1)	0.109(2)	1.1(3)	1.0
O4	8*f*	0.129(1)	0.4006(9)	0.328(2)	1.1(3)	1.0
O5	8*f*	0.225(1)	0.822(1)	0.317(2)	1.1(3)	1.0
O6	8*f*	0.3230(9)	0.505(1)	0.379(2)	1.1(3)	1.0

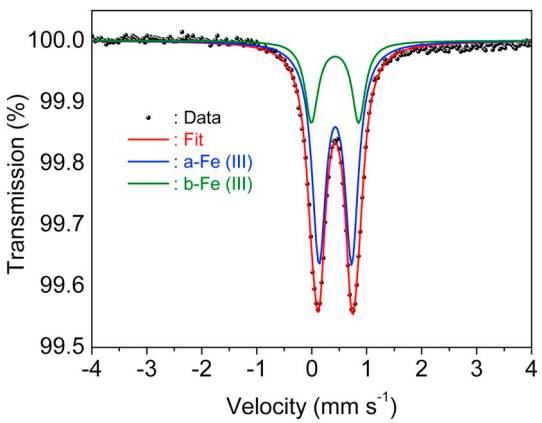

Fig. 3. ^{57}Fe Mossbauer spectrum of $Na_{1.5}\square_{0.5}Mn_{1.5}Fe_{1.5}(PO_4)_3$ recorded at room temperature.

Table 3
Fitted Mössbauer parameters[a] of $Na_{1.5}\square_{0.5}Mn_{1.5}Fe_{1.5}(PO_4)_3$ recorded at room temperature.

NMFP compound		δ (mm/s)	Δ (mm/s)	Γ (mm/s)	Area (%)
NMFP-700 °C	a-Fe(III)	0.43 (1)	0.60 (2)	0.30 (2)	74 (1)
	b-Fe(III)	0.42 (1)	0.86 (4)	0.28 (4)	26 (1)

[a] δ-Isomer shift, referred to α-iron at 295 K, Δ-quadrupole splitting, Γ-line width.

with XRD results, *which confirms the high purity of the sample*.

Good quality fit of the $Na_{1.5}\square_{0.5}Mn_{1.5}Fe_{1.5}(PO_4)_3$ spectrum has been obtained by using only two doublets; however, the XRD results of the $Na_{1.5}\square_{0.5}Mn_{1.5}Fe_{1.5}(PO_4)_3$ material shows that Fe^{3+} only occurs on the M(2) site. The presence of two doublets reflects the distribution of next-nearest-neighbor interactions due to chemical disorder on adjacent M (2) octahedral sites occupied by Mn, Fe and vacancies. Such interactions were previously reported in alluaudite-type phosphates; the isomer shift and quadrupole splitting values observed here are in good agreement with those from the literature [29–31]. The obtained values of the isomer shift are similar for the two doublets: $\delta \approx 0.42\ mm{\cdot}s^{-1}$, which is characteristic of high spin Fe^{3+} in FeO_6-type octahedral sites in agreement with both XRD and magnetic measurements (Table 1). Even if iron occurs only on the M(2) site, two pronouncedly inequivalent surroundings of iron sites can be distinguished, induced by a random distribution of Fe^{3+} and Mn^{2+} at the M(2) sites while the M(1) sites are filled with only Mn^{2+}. Indeed, the two sub-spectra clearly differ by the values of the quadrupole splitting, Δ(a-Fe (III)) = $0.60\ mm{\cdot}s^{-1}$ and Δ(b-Fe(III)) = $0.68\ mm{\cdot}s^{-1}$. The calculation of distribution probabilities indicates that the Fe^{3+}-Fe^{3+} configuration should involve 75% of Fe^{3+}, while the Fe^{3+}-Mn configuration should involve 25% of Fe^{3+}. Consequently, doublet a, with 74% area, corresponds to the Fe^{3+}-Fe^{3+} configuration, while doublet b, with 26% area, corresponds to the Fe^{3+}-Mn configuration.

3.3. Magnetic measurements

The inverse magnetic susceptibility of $Na_{1.5}\square_{0.5}Mn_{1.5}Fe_{1.5}(PO_4)_3$ measured in ZFC and FC are very close, showing paramagnetic behavior in a large temperature range and no magnetic impurities (Fig. 4). These results are consistent with XRD and Mössbauer spectroscopy. The values of the Curie temperature obtained from the linear fitting to the data

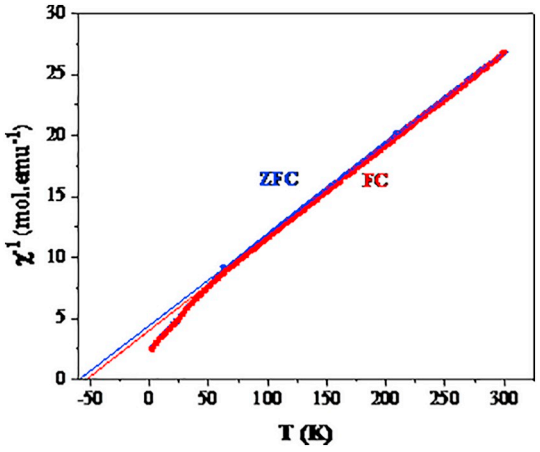

Fig. 4. Temperature dependence of the inverse magnetic susceptibility of $Na_{1.5}\square_{0.5}Mn_{1.5}Fe_{1.5}(PO_4)_3$ measured in ZFC (blue circles) and FC (red squares). The blue and red lines are extrapolation lines obtained from ZFC and FC data, respectively, in the temperature range 150–300 K. (For interpretation of the references to colour in this figure legend, the reader is referred to the web version of this article.)

in the temperature range 150–300 K are −59 and −53 K for ZFC and FC measurements, respectively, indicating antiferromagnetic order at low temperature. The values of the Curie constant are C = 13.40 and 13.20 emu K mol^{-1} for ZFC and FC measurements, respectively. The effective magnetic moment obtained from these values is $\mu_{eff} = 10.3\ \mu_B$ per formula unit (f.u.). The Mössbauer spectroscopy revealed the existence of only high spin Fe^{3+} that has a spin-only moment of 5.92 μ_B. By assuming the existence of only high spin Mn^{2+} ions that have the same spin-only moment, we obtain for the nominal composition $Na_{1.5}\square_{0.5}Mn_{1.5}Fe_{1.5}(PO_4)_3$ the theoretical effective spin-only moment of 10.3 μ_B per f.u. and for the structural composition $Na_{1.63}\square_{0.52}Mn_{1.35}Fe_{1.5}(PO_4)_3$ the value of 10.0 μ_B per f.u. that are both in excellent agreement with the experimental value. Thus, the magnetic measurements are consistent with the existence of only Fe^{3+} and Mn^{2+} oxidation states and confirm the absence of Fe^{2+} in agreement with Mössbauer measurements.

3.4. Morphological analyses

To clarify the microstructure, scanning electron microscopy (SEM) images of the $Na_{1.5}\square_{0.5}Mn_{1.5}Fe_{1.5}(PO_4)_3$ microrods were taken (Fig. 5) and further investigated. The SEM images (Fig. 5a and b) reveal that all particles are constituted of uniform $Na_{1.5}\square_{0.5}Mn_{1.5}Fe_{1.5}(PO_4)_3$ microrods characterized by homogeneously distributed sizes with an average length of about 3–6 μm. The high magnification image (Fig. 5c) shows that the single microrods are formed by nanoparticles of about 200–500 nm. This particle morphology is a consequence of the specific nucleation and crystal growth conditions in the solvothermal bomb [32]. The samples show low agglomeration of the particles, this increases the contact area between grains and electrolyte, which improves the electrochemical performances [33]. The synthesis in ethylene glycol prevented the $Na_{1.5}\square_{0.5}Mn_{1.5}Fe_{1.5}(PO_4)_3$ particles growth.

In order to clarify the effect of annealing process, the changes in structure and morphology of the samples were studied before and after the annealing process. Fig. 6 shows the comparison of XRD patterns and SEM images before and after the annealing process. The comparison between XRD patterns shows peaks at close positions for both samples, however it is clear that the annealed sample shows narrower XRD peaks than the as-prepared sample. This justifies the highly crystallinity achieved during the annealing process. The particles morphology measurements characterized by SEM suggest that heat treatment step at 700 °C removes the solvent incorporated in the crystal and increases the crystallinity of the $Na_{1.5}\square_{0.5}Mn_{1.5}Fe_{1.5}(PO_4)_3$ sample, but does not affect the particle crystal structure or the particle morphology.

3.5. Electrochemical measurements

Electrochemical measurements were carried out in lithium half-cell configuration. In the following sections, $Na_{1.5}\square_{0.5}Mn_{1.5}Fe_{1.5}(PO_4)_3$ material is evaluated as dual electrode material for Li-ion batteries. The evaluation of the electrochemical applicability of the $Na_{1.5}\square_{0.5}Mn_{1.5}Fe_{1.5}(PO_4)_3$ particles in Li-ion batteries was investigated using a Swagelok cell configuration. The theoretical capacity of $Na_{1.5}\square_{0.5}Mn_{1.5}Fe_{1.5}(PO_4)_3$ used as positive electrode is $110\ mAh{\cdot}g^{-1}$ for 2 e^- reaction [6,34,35]. When $Na_{1.5}\square_{0.5}Mn_{1.5}Fe_{1.5}(PO_4)_3$ is used as negative electrode, the theoretical capacity is $414\ mAh{\cdot}g^{-1}$, by considering 7.5 e^- reaction.

3.5.1. $Na_{1.5}\square_{0.5}Mn_{1.5}Fe_{1.5}(PO_4)_3$ as cathode material

The electrochemical performances of $Na_{1.5}\square_{0.5}Mn_{1.5}Fe_{1.5}(PO_4)_3$ as cathode material for Li-ion batteries were evaluated in a half-cell with lithium metal as counter electrode in the potential window: 1.5–4.5 V vs. Li/Li^+. Cyclic voltammograms (CV) were obtained at a scan rate of $0.5\ mV.s^{-1}$. As shown in Fig. 7a, during the first charge, there is a peak at about 3.3 V at the CV curve, which may correspond to the de-intercalation of Na^+ and the oxidation of Mn^{2+} in the structure [36]. The

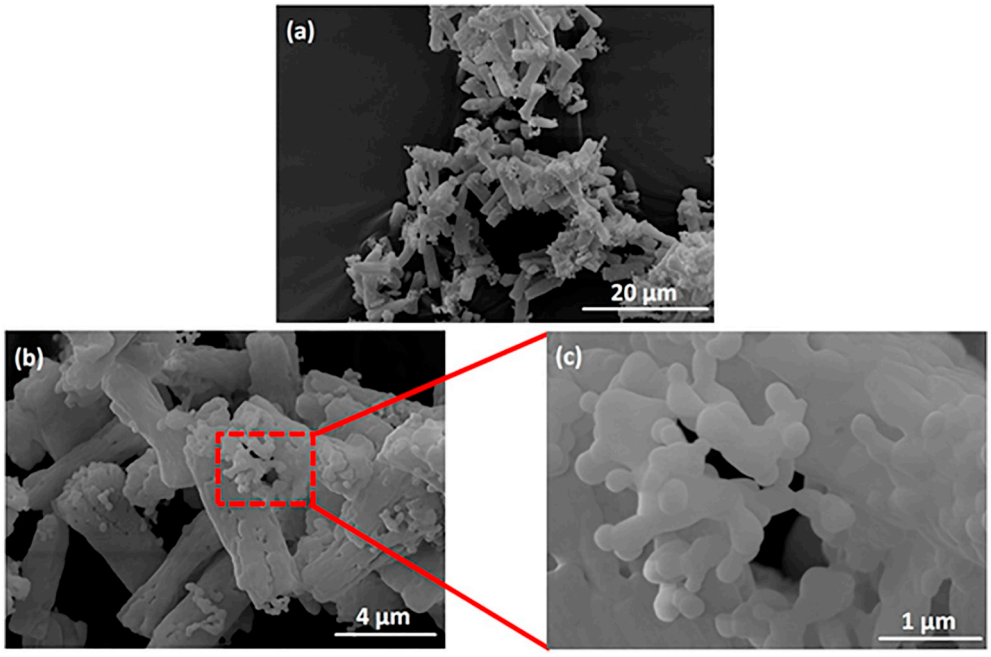

Fig. 5. (a, b and c) SEM of micrographs of $Na_{1.5}\square_{0.5}Mn_{1.5}Fe_{1.5}(PO_4)_3$ sample calcined under air at 700 °C.

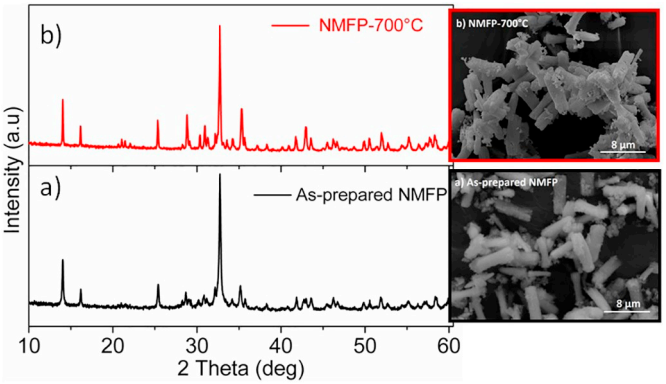

Fig. 6. XRD patterns and SEM images of a) as prepared $Na_{1.5}\square_{0.5}Mn_{1.5}Fe_{1.5}(PO_4)_3$ and b) calcined $Na_{1.5}\square_{0.5}Mn_{1.5}Fe_{1.5}(PO_4)_3$ material at 700 °C.

galvanostatic voltage profiles were measured at the different current densities of 5, 20, 50 and 100 $mA{\cdot}g^{-1}$ (Fig. 7b). The charge/discharge curves (Fig. 7b) show that a high reversible capacity of about 107 $mAh{\cdot}g^{-1}$ at 5 $mA{\cdot}g^{-1}$ was achieved, which corresponds to deintercaltion/intercalation of about 1.94 Li^+ ions per formula unit.

The capacity drops upon increasing the applied current density that is accompanied by decrease of the working voltage. Indeed, the cell shows continuous voltage and polarization changes upon cycling especially at high current densities. The shape of the voltage curves is similar for all current densities, showing good reversible Li-insertion/deinsertion processes in the electrode materials with relatively good specific capacities at different current densities.

The rate capability helps to examine whether or not a kinetic limitation of lithium-ion transfer in the solid is present. Fig. 8a shows the rate charge/discharge performances of $Na_{1.5}\square_{0.5}Mn_{1.5}Fe_{1.5}(PO_4)_3$ electrode material under different current densities from 5 to 100 mA g^{-1}. The cathode material delivers specific capacities of 107, 65, 48, and 35 $mAh{\cdot}g^{-1}$ at the current densities of 5, 20, 50, and 100 $mA{\cdot}g^{-1}$, respectively. When the current density is changed back to

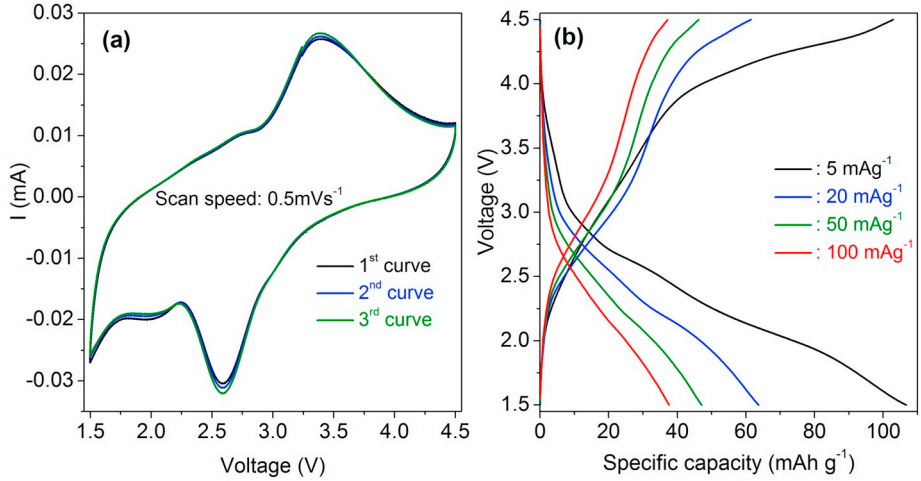

Fig. 7. a) Cyclic voltammetry (CV) profiles $Na_{1.5}\square_{0.5}Mn_{1.5}Fe_{1.5}(PO_4)_3$ between 1.5 and 4.5 V (vs. Li/Li^+). **b)** Charge/discharge curves of $Na_{1.5}\square_{0.5}Mn_{1.5}Fe_{1.5}(PO_4)_3$ between 1.5 and 4.5 V (vs. Li/Li^+) at different current densities.

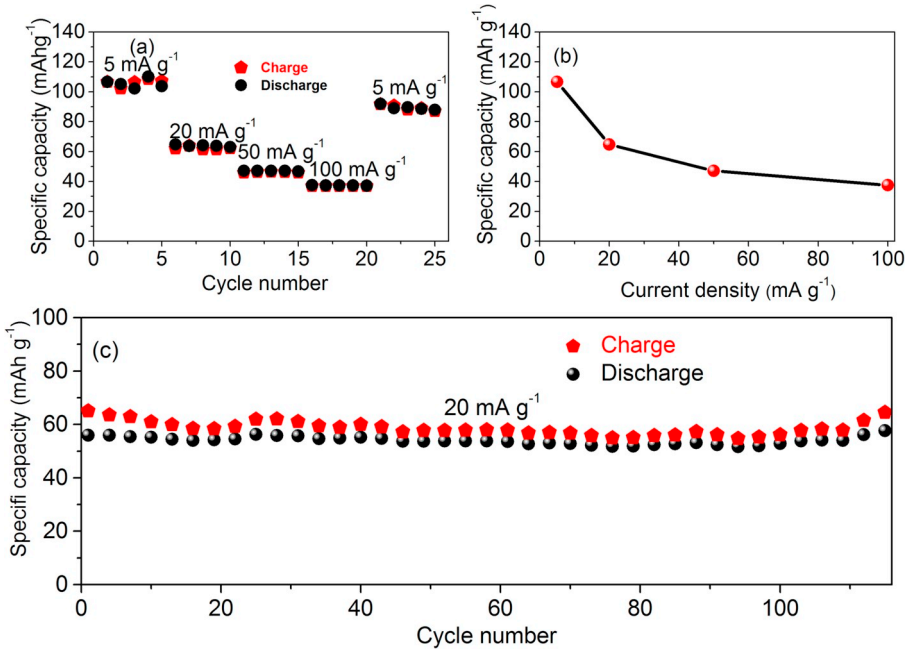

Fig. 8. Electrochemical performances of $Na_{1.5}\square_{0.5}Mn_{1.5}Fe_{1.5}(PO_4)_3$ as cathode material for lithium-ion batteries: (a) rate capability, (b) evolution of discharge capacity as a function of current density; c) evolution of discharge/charge capacity vs. cycle number at current density of 20 mA·g^{-1}.

5 mA·g^{-1} after 25 cycles at various current densities, the reversible capacity resumes to 92 mAh·g^{-1}. The capacity fade may be due to the large particle size and low electronic and ionic conductivity.

The specific capacity decreases with increasing discharge current density (Fig. 8b) but this may be resolved by increasing particle surface area through reduction of particle size or by carbon coating to enhance ionic and electronic conductivities of the cathode material [7,37,38].

In Fig. 8c, the evolution of discharge and charge capacities vs. cycle number at 20 mA.g^{-1} charge/discharge rates is presented. After continuous cycling for about 115 cycles at a current density of 20 mA·g^{-1}, a reversible discharge capacity of about 65 mAh·g^{-1} is retained, corresponding to 99.1% of the initial cycle discharge capacity. This shows that $Na_{1.5}\square_{0.5}Mn_{1.5}Fe_{1.5}(PO_4)_3$ is characterized by an excellent cycling performance.

3.5.2. $Na_{1.5}\square_{0.5}Mn_{1.5}Fe_{1.5}(PO_4)_3$ as anode material

Fig. 9a shows cyclic voltammograms (CV) of $Na_{1.5}\square_{0.5}Mn_{1.5}Fe_{1.5}(PO_4)_3$ as anode material in the voltage range of 0.03–3.0 V at 0.5 mV·s^{-1}. The first discharge curve is different than the other cycles and shows a pronounced peak at 0.3 V that could correspond to the $Fe^{3+/0}$, $Mn^{2+/0}$ redox couples, respectively. This indicates that the reaction occurring at the first discharge is irreversible which corresponds to the transformation of phosphate upon initial reaction with lithium. During the first charge, two small peaks around 1.1 and 1.85 V were detected, that may correspond to the partial oxidation of Fe^0 and Mn^0. The second discharge shows a principal peak at around 1.0 V. The typical galvanostatic profiles for lithium intercalation/extraction in $Na_{1.5}\square_{0.5}Mn_{1.5}Fe_{1.5}(PO_4)_3$ in the voltage window 0.03–3 V at 50 mA g^{-1} current density are shown in Fig. 9b. The theoretical capacity (~414 mAh·g^{-1}) value of the $Na_{1.5}\square_{0.5}Mn_{1.5}Fe_{1.5}(PO_4)_3$ as negative electrode is equivalent to the intercalation of 7.5 Li^+ ions, expected for the reduction of Fe^{3+} to Fe^0 and Mn^{2+} to Mn^0 per formula unit. The sample delivers an irreversible capacity of 675 mAh·g^{-1} during the first discharge, which is higher than the theoretical capacity. The origin of the additional contribution is still unclear although one can suspect that the presence of vacancies in the material structure, the

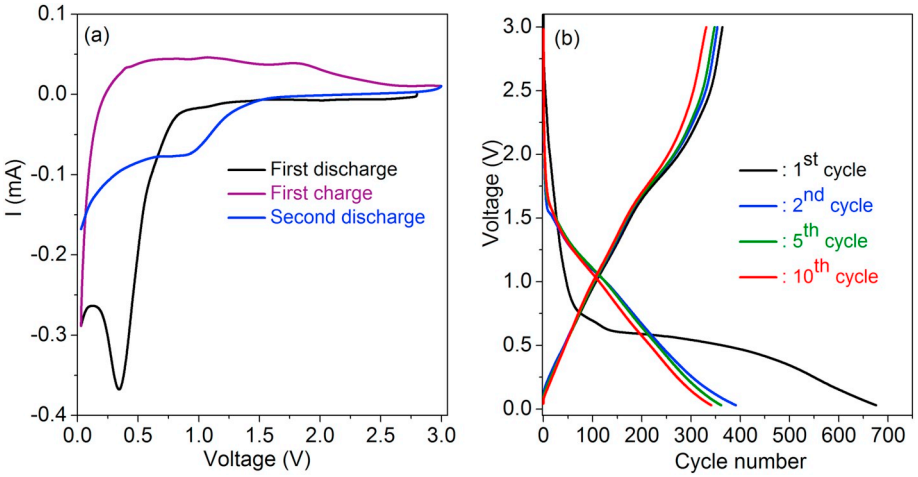

Fig. 9. a) Cyclic voltammetry (CV) profiles of $Na_{1.5}\square_{0.5}Mn_{1.5}Fe_{1.5}(PO_4)_3$ between 0.03 and 3.0 V (vs. Li/Li$^+$). **b)** Charge-discharge curves and at 50 mA g^{-1} current density for $\square_{0.5}Na_{1.5}Mn_{1.5}Fe_{1.5}(PO_4)_3$ as anode material in the voltage window of 0.03–3.0 V vs. Li^+/Li^0.

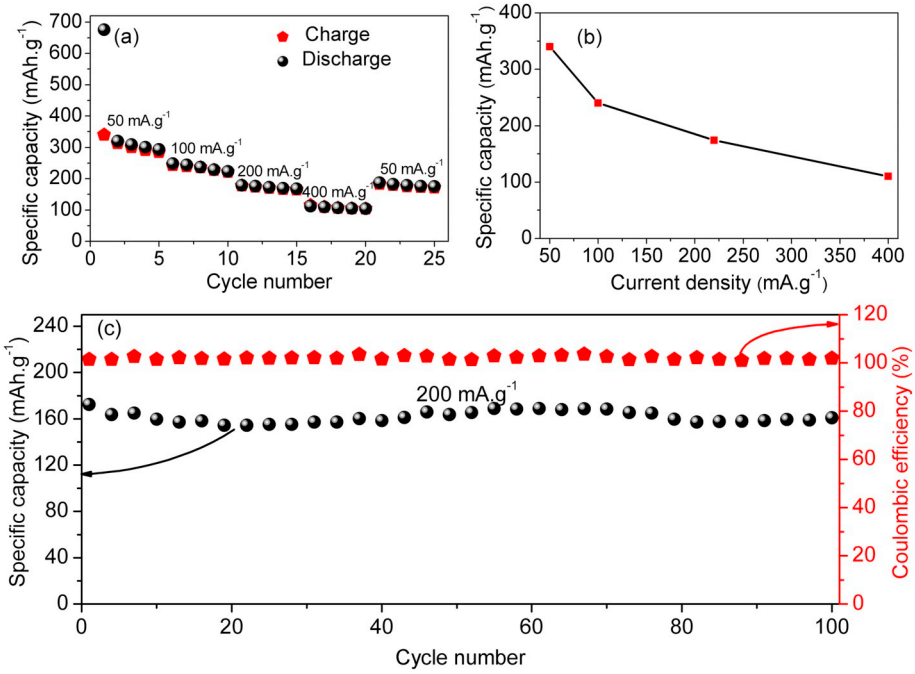

Fig. 10. Electrochemical evaluation of $Na_{1.5}\square_{0.5}Mn_{1.5}Fe_{1.5}(PO_4)_3$ as anode material for lithium-ion batteries: (a) rate capability; (b) evolution of discharge capacity as a function of current density; c) evolution of discharge/charge capacity vs. cycle number at current density of 200 mA·g^{-1}.

reduction of the electrolyte over the material–carbon interface, the electrolyte decomposition and the formation of the SEI at the electrode interface may contribute to the extra capacity at the initial cycle as possible mechanisms [26,27]. Dual electrode materials are interesting in rechargeable battery field because a single-batch preparation can be used for the two electrodes (positive and negative). The reversible discharge capacity of about 390 mAh·g^{-1} was obtained at second cycle at 50 mA·g^{-1}. This large irreversible capacity loss and the differences between the potential profiles of the first and following discharges suggest intercalation/conversion reaction mechanism during the first discharge. The analysis of the potential curve of the first discharge signals an intriguing behavior corresponding to the appearance of three pseudo-plateaus. The small plateau in first discharge curve, observed at about 0.75 V may correspond to the reduction of Fe^{3+} to Fe^{2+}. The plateau observed between 0.5 and 0.6 V voltage could be due to the reduction of the electrolyte leading to the SEI formation [39]. *This could also be due to the reduction of $Fe^{2+/0}$ and $Mn^{2+/0}$ as previously observed for iron in oxyphosphates $M_{0.5}TiOPO_4$ (M: Ni, Co and Fe)* [40–44] *and for the reduction action of Mn^{2+} to metallic Mn that occurs near 0.2 V* [45].

Fig. 10a shows that $Na_{1.5}\square_{0.5}Mn_{1.5}Fe_{1.5}(PO_4)_3$ as negative electrode delivers an average reversible specific capacity of 340, 240, 174 and 110 mAh·g^{-1} in 0.03–3.0 V voltage window at current densities of 50, 100, 200, and 400 mA·g^{-1}, respectively.

The obtained specific capacity as a function of the discharge current density is plotted in Fig. 10b. After continuous cycling for 100 cycles at 200 mA.g^{-1}, an average reversible discharge capacity as high as 170 mAh·g^{-1} is retained (Fig. 10c). This shows that $Na_{1.5}\square_{0.5}Mn_{1.5}Fe_{1.5}(PO_4)_3$ electrode possesses excellent cycling stability even for high current density. This results suggests that $Na_{1.5}\square_{0.5}Mn_{1.5}Fe_{1.5}(PO_4)_3$ as negative electrode material has good capability in hybrid battery.

These preliminary results show that $Na_{1.5}\square_{0.5}Mn_{1.5}Fe_{1.5}(PO_4)_3$ synthesized by an original solvothermal procedure exhibited good electrochemical properties (good rate capability and cycling stability), suggesting that, after optimizing the synthesis conditions for a better morphology and suitable size, $Na_{1.5}\square_{0.5}Mn_{1.5}Fe_{1.5}(PO_4)_3$ may be considered as a promising electrode material due to its excellent intercalation/deintercation of lithium especially as negative electrode. In the latter case, $Na_{1.5}\square_{0.5}Mn_{1.5}Fe_{1.5}(PO_4)_3$ could be also a good candidate for sodium-ion batteries since graphite does not intercalate sodium to any appreciable extent as reported in the literature [46].

Finally, the electrochemical performances of $Na_{1.5}\square_{0.5}Mn_{1.5}Fe_{1.5}(PO_4)_3$ based electrode material are compared with some recent results obtained for alluaudites used as electrode materials

Table 4
Comparison between the electrochemical performances of $Na_{1.5}\square_{0.5}Mn_{1.5}Fe_{1.5}(PO_4)_3$ and some recent results obtained for alluaudite materials used as electrode material for Li/Na-ion batteries.

References	Alluaudite material	Voltage Range (V)	Maximum specific capacity (mAh g^{-1}) and C-rate	Cycle number	QRt-N (%)	Comments
This work	$Na_{1.5}\square_{0.5}Mn_{1.5}Fe_{1.5}(PO_4)_3$	1.5–4.5	~107(C/20)	115	99.1% (C/4)	Cathode material for Na-ion batteries
This work	$Na_{1.5}\square_{0.5}Mn_{1.5}Fe_{1.5}(PO_4)_3$	0.03–3.0	350 (~C/10)	100	~99% (20 mA g^{-1})	Anode material for Na-ion batteries
[36]	$Li_{0.75}Mn_{1.50}Fe_{1.75}(PO_4)_3$	1.5–4.5	30 (C/50)	–	–	Cathode material for Li-ion batteries
[47]	$NaMnFe_2(PO_4)_3$	1.5–4.5	~60(C/20)	25	~100% (C/20)	Cathode material for Na-ion batteries
[48]	$Na_{2+2x}Fe_{2-x}(SO_4)_3$	2.0–4.5 V	90 (5C)	500	~89%	Reduced graphene oxide was added to enhance the electrochemical performance of the cathode material for Na-ion batteries
[49]	$Na_{2.4}Fe_{1.8}(SO_4)_3$	2.0–4.8	110 (C/10)	–	–	Cathode material for Li-ion batteries

for Li/Na-ion batteries [36,47–49]. Table 4 shows that $Na_{1.5}\square_{0.5}Mn_{1.5}Fe_{1.5}(PO_4)_3$ delivers the highest specific capacity as cathode material of 107 mAh.g^{-1} at 5 mA.g^{-1} with a very good capacity retention after 115 cycles at 20 mA·g^{-1}. As anode material, $Na_{1.5}\square_{0.5}Mn_{1.5}Fe_{1.5}(PO_4)_3$ shows excellent capacity retention during 100 cycles at 200 mA·g^{-1}. It should be noticed these performances were obtained without any optimization of the material (carbon addition, grinding, etc.) or of the electrolyte.

4. Conclusions

We have successfully synthesize $Na_{1.5}\square_{0.5}Mn_{1.5}Fe_{1.5}(PO_4)_3$ by solvothermal method, a new dual electrode material tested in lithium-ion battery. We have shown that the solvothermal synthesis is an appropriate method to prepare particles with suitable size and morphology for application as electrode materials for lithium-ion batteries. The composition and the structure were accurately determined by using ^{57}Fe Mössbauer spectroscopy, XRD Rietveld refinements and magnetic measurements. Rietveld refinements shows that vacancies occur on the A(2)' sites and Mossbauer spectroscopy shows the presence only of Fe^{3+} in the materials with two inequivalent surroundings. Magnetic measurements confirm the existence only of Fe^{3+} and Mn^{2+}. We have found that $Na_{1.5}\square_{0.5}Mn_{1.5}Fe_{1.5}(PO_4)_3$ has high capacities of ~110 and 390 mAh.g^{-1} as cathode and anode materials, respectively, good cyclability and rate capability. In brief, $Na_{1.5}\square_{0.5}Mn_{1.5}Fe_{1.5}(PO_4)_3$ is a very interesting material due to its dual electrode performance properties, especially its high capacity retention when it is cycled as anode material. It exhibits good lithium intercalation/extraction behavior even though no optimizations of particle size, morphology and/or carbon coating were performed. Because of its interesting properties, a structure including vacancies for insertion, dual electrochemical properties and high specific capacity $Na_{1.5}\square_{0.5}Mn_{1.5}Fe_{1.5}(PO_4)_3$ could be further developed and used as electrode material for sodium-ion batteries.

Acknowledgements

The authors are grateful to University of Liege and FRS-FNRS for equipment grants. Part of this work was supported by the Walloon Region under the "PE PlanMarshall2.vert" program (BATWAL–1318146). C. Karegeya acknowledges the abroad study leave of the University of Rwanda. A. Mahmoud is grateful to the Walloon region for a Beware Fellowship Academia 2015-1, RESIBAT n° 1510399. The authors are grateful to Corine Reibel for magnetic measurements.

References

[1] C. Nan, J. Lu, C. Chen, Q. Peng, Y. Li, Solvothermal synthesis of lithium iron phosphate nanoplates, J. Mater. Chem. 21 (2011) 9994–9996.
[2] M.K. Devaraju, I. Honma, Hydrothermal and solvothermal process towards development of $LiMPO_4$ (M = Fe, Mn) nanomaterials for lithium-ion batteries, Adv. Energy Mater. 2 (2012) 284–297.
[3] C. Karegeya, A. Mahmoud, B. Vertruyen, F. Hatert, R.P. Hermann, R. Cloots, F. Boschini, One-step hydrothermal synthesis and electrochemical performance of sodium-manganese-iron phosphate as cathode material for Li-ion batteries, J. Solid State Chem. 253 (2017) 389–397.
[4] S. Li, A. Li, R. Zhang, Y. He, Y. Zhai, L. Xu, Hierarchical porous metal ferrite ball-in-ball hollow spheres: general synthesis, formation mechanism, and high performance as anode materials for Li-ion batteries, Nano Res. 7 (2014) 1116–1127.
[5] W. Huang, B. Li, M.F. Saleem, X. Wu, J. Li, J. Lin, D. Xia, W. Chu, Z. Wu, Self-assembled alluaudite $Na_2Fe_{3-x}Mn_x(PO_4)_3$ micro/nanocompounds for sodium-ion battery electrodes: a new insight into their electronic and geometric structure, Chem. Eur. J. 21 (2015) 851–860.
[6] R. Essehli, H.B. Yahia, K. Maher, M.T. Sougrati, A. Abouimrane, J.-B. Park, Y.-K. Sun, M.A. Al-Maadeed, I. Belharouak, Unveiling the sodium intercalation properties in $Na_{1.86}\square_{0.14}Fe_3(PO_4)_3$, J. Power Sources 324 (2016) 657–664.
[7] C. Karegeya, A. Mahmoud, R. Cloots, B. Vertruyen, F. Boschini, Hydrothermal synthesis in presence of carbon black: particle-size reduction of iron hydroxyl phosphate hydrate for Li-ion battery, Electrochim. Acta 250 (2017) 49–58.
[8] S. Han, J. Wang, S. Li, D. Wu, X. Feng, Graphene aerogel supported $Fe_5(PO_4)_4(OH)_3{\cdot}2H_2O$ microspheres as high performance cathode for lithium ion batteries, J. Mater. Chem. A 2 (2014) 6174–6179.
[9] M. Brisbois, S. Caes, M.T. Sougrati, B. Vertruyen, A. Schrijnemakers, R. Cloots, N. Eshraghi, R.P. Hermann, A. Mahmoud, F. Boschini, Na_2FePO_4F/multi-walled carbon nanotubes for lithium-ion batteries: Operando Mössbauer study of spray-dried composites, Sol. Energy Mater. Sol. Cells 148 (2016) 67–72.
[10] A. Mahmoud, S. Caes, M. Brisbois, R.P. Hermann, L. Berardo, A. Schrijnemakers, C. Malherbe, G. Eppe, R. Cloots, B. Vertruyen, F. Boschini, Spray-drying as a tool to disperse conductive carbon inside Na_2FePO_4F particles by addition of carbon black or carbon nanotubes to the precursor solution, J. Solid State Electrochem. (2017) 1–10.
[11] F. Hatert, Crystal chemistry of the divalent cation in alluaudite-type phosphates: a structural and infrared spectral study of the $Na_{1.5}(\ )_{1.5}Fe_{1.5}(PO_4)_3$ solid solutions (x = 0 to 1, M^{2+} = Cd^{2+}, Zn^{2+}), J. Solid State Chem. 181 (2008) 1258–1272.
[12] F. Hatert, The crystal chemistry of lithium in the alluaudite structure: a study of the $(Na_{1-x}Li_x)_{1.5}Mn_{1.5}Fe_{1.5}(PO_4)_3$ solid solution (x = 0 to 1), Mineral. Petrol. 81 (2004) 205–217.
[13] D. Jugović, D. Uskoković, A review of recent developments in the synthesis procedures of lithium iron phosphate powders, J. Power Sources 190 (2009) 538–544.
[14] P. Benedek, N. Wenzler, M. Yarema, V.C. Wood, Low temperature hydrothermal synthesis of battery grade lithium iron phosphate, RSC Adv. 7 (2017) 17763–17767.
[15] M. Yoshimura, K. Byrappa, Hydrothermal processing of materials: past, present and future, J. Mater. Sci. 43 (2008) 2085–2103.
[16] C. Masquelier, L. Croguennec, Polyanionic (phosphates, silicates, sulfates) frameworks as electrode materials for rechargeable Li (or Na) batteries, Chem. Rev. 113 (2013) 6552–6591.
[17] M.-K. Devaraju, I. Honma, Hydrothermal and solvothermal process towards development of LiMPO4 (M = Fe, Mn) nanomaterials for lithium-ion batteries, Adv. Energy Mater. 2 (2012) 284–297.
[18] X. Liu, J.-Q. Huang, Qi. Zhang, X.-Y. Liu, H.-J. Peng, W. Zhu, F. Wei, N-Methyl-2-pyrrolidone-assisted solvothermal synthesis of nanosize orthorhombic lithium iron phosphate with improved Li-storage performance, J. Mater. Chem. 22 (2012) 18908–18914.
[19] C. Zhu, Z. Wu, J. Xiea, Z. Chen, J. Tu, G. Cao, X. Zhao, Solvothermal-assisted morphology evolution of nanostructuredLiMnPO4as high-performance lithium-ion batteries cathode, J. Mater. Sci. Technol. 34 (2018) 1544–1549.
[20] S. Yu, A. Mertens, R. Schierholz, H. Tempel, Rüdiger A. Eichel, Morphology dependency of $Li_3V2(PO4)_3$/C cathode material regarding to rate capability and cycle life in Lithium-ion batteries, Electrochim. Acta 232 (2017) 310–322.
[21] S. Yang, X. Zhou, J. Zhang, Z. Liu, Morphology-controlled solvothermal synthesis of $LiFePO_4$ as a cathode material for lithium-ion batteries, J. Mater. Chem. 20 (2010) 8086–8091.
[22] J. Lim, S.-W. Kang, J. Moon, S. Kim, H. Park, J.P. Baboo, J. Kim, Low-temperature synthesis of $LiFePO_4$ nanocrystals by solvothermal route, Nanoscale Res. Lett. 7 (2012) 3.
[23] D. Liu, G. Cao, Engineering nanostructured electrodes and fabrication of film electrodes for efficient lithium ion intercalation, Energy Environ. Sci. 3 (2010) 1218–1237.
[24] A. Mahmoud, J.M. Amarilla, K. Lasri, I. Saadoune, Influence of the synthesis method on the electrochemical properties of the $Li_4Ti_5O_{12}$ spinel in Li-half and Li-ion full-cells. A systematic comparison, Electrochim. Acta 93 (2013) 163–172.
[25] X. Qin, J. Wang, J. Xie, F. Li, L. Wen, X. Wang, Hydrothermally synthesized $LiFePO_4$ crystals with enhanced electrochemical properties: simultaneous suppression of crystal growth along [010] and antisite defect formation, Phys. Chem. Chem. Phys. 14 (2012) 2669–2677.
[26] R. Essehli, I. Belharouak, H.B. Yahia, R. Chamoun, B. Orayech, B. El Bali, K. Bouziane, X.L. Zhou, Z. Zhou, α-$Na_2Ni_2Fe(PO_4)_3$: a dual positive/negative electrode material for sodium ion batteries, Dalton Trans. 44 (2015) 4526–4532.
[27] R. Essehli, I. Belharouak, H.B. Yahia, K. Maher, A. Abouimrane, B. Orayech, S. Calder, X.L. Zhou, Z. Zhou, Y.K. Sun, Alluaudite $Na_2Co_2Fe(PO_4)_3$ as an electroactive material for sodium ion batteries, Dalton Trans. 44 (2015) 7881–7886.
[28] A. Mahmoud, J.M. Amarilla, I. Saadoune, Effect of thermal treatment used in the sol–gel synthesis of $Li_4Ti_5O_{12}$ spinel on its electrochemical properties as anode for lithium ion batteries, Electrochim. Acta 163 (2015) 213–222.
[29] F. Hatert, L. Rebbouh, R.P. Hermann, A.-M. Fransolet, G.J. Long, F. Grandjean, Crystal chemistry of the hydrothermally synthesized $Na_2(Mn_{1-x}Fe_x^{2+})_2Fe^{3+}(PO_4)_3$ alluaudite-type solid solution, Am. Mineral. 90 (2005) 653–662.
[30] R.P. Hermann, F. Hatert, A.-M. Fransolet, G.J. Long, F. Grandjean, Mössbauer spectral evidence for next-nearest neighbor interactions within the alluaudite structure of $Na_{1-x}Li_xMnFe_2(PO_4)_3$, Solid State Sci. 4 (2002) 507–513.
[31] F. Hatert, G.J. Long, D. Hautot, A.-M. Fransolet, J. Delwiche, M.-J. Hubin-Franskin, F. Grandjean, A structural, magnetic, and Mössbauer spectral study of several Na–Mn–Fe-bearing alluaudites, Phys. Chem. Miner. 31 (2004) 487–506.
[32] C. Karegeya, A. Mahmoud, B. Vertruyen, F. Hatert, R. Cloots, F. Boschini, Hydrothermal self-assembly of sodium manganese iron phosphate particles: growth mechanism and electrochemical performance in lithium-ion battery, Solid State Ionics 312 (2017) 88–96.
[33] A. Mahmoud, I. Saadoune, P.-E. Lippens, M. Chamas, R. Hakkou, J.M. Amarilla, The design and study of new Li-ion full cells of $LiCo_{2/3}Ni_{1/6}Mn_{1/6}O_2$ positive electrode paired with $MnSn_2$ and $Li_4Ti_5O_{12}$ negative electrodes, Solid State Ionics 300 (2017) 175–181.
[34] K. Trad, D. Carlier, L. Croguennec, A. Wattiaux, M. Ben Amara, C. Delmas, $NaMnFe_2(PO_4)_3$ alluaudite phase: synthesis, structure, and electrochemical properties as positive electrode in lithium and sodium batteries, Chem. Mater. 22 (2010) 5554–5562.
[35] V. Palomares, P. Serras, I. Villaluenga, K.B. Hueso, J. Carretero-González, T. Rojo,

Na-ion batteries, recent advances and present challenges to become low cost energy storage systems, Energy Environ. Sci. 5 (2012) 5884–5901.
[36] K. Trad, A. Castets, A. Wattiaux, C. Delmas, M. Ben Amara, D. Carlier, J. Solid State Chem. 265 (2018) 12–17.
[37] N. Eshraghi, S. Caes, A. Mahmoud, R. Cloots, B. Vertruyen, F. Boschini, Sodium vanadium (III) fluorophosphate/carbon nanotubes composite (NVPF/CNT) prepared by spray-drying: good electrochemical performance thanks to well-dispersed CNT network within NVPF particles, Electrochim. Acta 228 (2017) 319–324.
[38] Rui Ling, Shu Cai, Sibo Shen, Xudong Hu, Dongli Xie, Feiyang Zhang, Xiaohong Sun, Nian Yu, Fengwu Wang, Synthesis of carbon coated $Na_2FePO4F$ as cathode materials for high performance sodium ion batteries, J. Alloys Compd. 704 (2017) 631–640.
[39] A. Mahmoud, M. Chamas, P.-E. Lippens, Electrochemical impedance study of the solid electrolyte interphase in $MnSn_2$ based anode for Li-ion batteries, Electrochim. Acta 184 (2015) 387–391.
[40] I. Belharouak, K. Amine, New active titanium oxyphosphate material for lithium batteries, Electrochem. Commun. 7 (2005) 648–651.
[41] K. Lasri, I. Saadoune, Y. Bentaleb, D. Mikhailova, H. Ehrenberg, L. Häggström, K. Edström, Origin of the irreversible capacity of the $Fe_{0.5}TiOPO_4$ anode material, Solid State Ionics 224 (2012) 15–20.
[42] R. Essehli, B. El Bali, A. Faik, M. Naji, S. Benmokhtar, Y.R. Zhong, L.W. Su, Z. Zhou, J. Kim, K. Kang, et al., Iron titanium phosphates as high-specific-capacity electrode materials for lithium ion batteries, J. Alloys Compd. 585 (2014) 434–441.
[43] R. Essehli, B. El Bali, A. Faik, S. Benmokhtar, B. Manoun, Y. Zhang, X.J. Zhang, Z. Zhou, H. Fuess, Structural changes upon lithium insertion in $Ni_{0.5}TiOPO_4$, J. Alloys Compd. 530 (2012) 178–185.
[44] C. Karegeyaa, A. Mahmoud, F. Hatert, B. Vertruyen, R. Cloots, P.E. Lippensd, F. Boschini, $Na_{1.25}Ni_{1.25}Fe_{1.75}(PO_4)_3$ nanoparticles as a janus electrode material for Li-ion batteries, J. Power Sour. 388 (2018) 57–64.
[45] H. Su, Y.-F. Xu, S.-C. Feng, Z.-G. Wu, X.-P. Sun, C.-H. Shen, J.- Wang, J.-T. Li, L. Huang, S.-G. Sun, Hierarchical Mn_2O_3 hollow microspheres as anode material of lithium ion battery and its conversion reaction mechanism investigated by XANES, ACS Appl. Mater. Interfaces 7 (2015) 8488–8494.
[46] M.D. Slater, D. Kim, E. Lee, C.S. Johnson, Sodium-ion batteries, Adv. Funct. Mater. 23 (2013) 947–958.
[47] D. Dwibedi, P.W. Jaschin, R. Gond, P. Barpanda, Revisiting the alluaudite $NaMnFe_2(PO_4)_3$ sodium insertion material: Structural, diffusional and electrochemical insights, Electrochim. Acta 283 (2018) 850–857.
[48] M. Zhang, H. Qi, H. Qiu, T. Zhang, X. Zhao, H. Yue, G. Chen, C. Wang, Y. Wei, D. Zhang, Reduced graphene oxide wrapped alluaudite $Na_{2+2x}Fe_{2-x}(SO_4)_3$ with high rate sodium ion storage properties, J. Alloys Compd. 752 (2018) 267–273.
[49] J. Ming, P. Barpanda, S.-I. Nishimura, M. Okubo, A. Yamada, An alluaudite $Na_{2+2x}Fe_{2-x}(SO_4)_3$(x = 0.2) derivative phase as insertion host for lithium battery, Electrochem. Commun. 51 (2015) 19–22.